Energy & Environmental Science

ROYAL SOCIETY OF CHEMISTRY

PAPER

View Article Online
View Journal

Check for updates

Cite this: DOI: 10.1039/d2ee03924a

Giant transverse thermoelectric effect induced by topological transition in polycrystalline Dirac semimetal Mg_3Bi_2†

Tao Feng, ‡[a] Panshuo Wang,‡[b] Zhijia Han,[a] Liang Zhou,[b] Zhiran Wang,[a] Wenqing Zhang,*[a] Qihang Liu*[b] and Weishu Liu *[ac]

Received 6th December 2022,
Accepted 8th February 2023

DOI: 10.1039/d2ee03924a

rsc.li/ees

To achieve thermoelectric energy conversion, a large transverse thermoelectric effect in topological materials is crucial. However, a simple and effective way to manipulate the performance of transverse thermoelectric materials still remains elusive. Herein, we demonstrate a topological transition-induced giant transverse thermoelectric effect in polycrystalline Mn-doped $Mg_{3+\delta}Bi_2$ material, which has a competitively large transverse thermopower (617 μV K^{-1}), power factor (20 393 μW m^{-1} K^{-2}), magnetoresistance (16 600%), and electronic mobility (35 280 cm^2 V^{-1} s^{-1}). The high performance is triggered by the modulation of the negative chemical pressure and disorder effects in the presence of Mn doping, which induces the transition from a topological insulator to a Dirac semimetal. The high-performance polycrystalline Mn-doped $Mg_{3+\delta}Bi_2$ described in this work robustly boosts the transverse thermoelectric effect through topological phase transition, paving a new avenue for the material design of transverse thermoelectricity.

Published on 10 February 2023. Downloaded by SUSTech on 3/1/2023 1:30:54 AM.

Broader context

In thermoelectric energy conversion, transverse geometry and a large transverse thermoelectric effect facilitate module fabrication. Single-crystal topological semimetals (*e.g.* $ZrTe_5$, NbP) have shown promise for achieving high transverse thermopower; however, the synthesis technology is difficult and the resulting sample batches are small, which is problematic for large-scale applications. Polycrystalline semimetals are easier to manufacture at scale but have previously failed to reproduce the performance of the single crystals. Here, we combine the benefits of performance and manufacturability to demonstrate that polycrystalline Mn-doped Mg_3Bi_2 has a large transverse thermopower (617 μV K^{-1}), power factor (20 393 μW m^{-1} K^{-2}) comparable to the state-of-the-art single-crystal materials, and also high magnetoresistance (16 600%) and electronic mobility (35 280 cm^2 V^{-1} s^{-1} at 2 K), which outperform undoped polycrystalline Mg_3Bi_2 by 17 times and 7 times, respectively. The significant enhancement of the transverse thermoelectric effects is triggered by the modulation of the negative chemical pressure and disorder effect in the presence of Mn doping, which alters the topological phase transition from a Z_2-like topological insulator to a Dirac semimetal. The discovery of high-performance polycrystalline Mn-doped Mg_3Bi_2 opens up new possibilities for the material design and device application of transverse thermoelectricity.

1. Introduction

Transverse thermoelectricity based on the Nernst effect has proven to be compelling for application in energy harvesting technology.[1–3] A voltage drop is generated along the direction perpendicular to the temperature gradient as a magnetic field is applied in the normal direction of the vector plane of the temperature gradient and voltage drop.[4] Such a scenario is not only conducive to decoupling electron and phonon transport, but also helpful in simplifying thermoelectric devices.[5,6] At present, most of the reported transverse thermoelectric materials belong to the category of topological semimetal with high carrier mobility, which is very different from the classic thermoelectric semiconductor, which is confined to a narrow

[a] Department of Materials Science and Engineering, Southern University of Science and Technology, Shenzhen 518055, China. E-mail: liuws@sustech.edu.cn, zhangwq@sustech.edu.cn
[b] Department of Physics and Shenzhen Institute for Quantum Science & Engineering, Southern University of Science and Technology, Shenzhen 518055, China. E-mail: liuqh@sustech.edu.cn
[c] Guangdong Provincial Key Laboratory of Functional Oxide Materials and Devices, Southern University of Science and Technology, Shenzhen 518055, China

† Electronic supplementary information (ESI) available. See DOI: https://doi.org/10.1039/d2ee03924a

‡ Tao Feng and Panshuo Wang contributed equally to this work.

Published on 10 February 2023. Downloaded by SUSTech on 3/1/2023 1:30:54 AM.

band gap.[7–14] For example, the topological Dirac semimetal $ZrTe_5$ was shown to have a high electron mobility ($<64\,000$ $cm^2\ V^{-1}\ s^{-1}$), leading to an evident transverse thermoelectric effect with a robust transverse power factor (10 314 $\mu W\ m^{-1}\ K^{-2}$ at 115 K).[7] Similarly, the Dirac semimetal Cd_3As_2 is known to have a large transverse thermopower (115 $\mu V\ K^{-1}$) and power factor (5000 $\mu W\ m^{-1}\ K^{-2}$ at 350 K), largely due to the charge compensation of pertinent electrons and holes and their high mobilities.[8,9] A third alternative, the Weyl semimetal NbP, has also exhibited strong transverse thermoelectric responses (800 $\mu V\ K^{-1}$ at 109 K) and ultra-high carrier mobility (5×10^6 $cm^2\ V^{-1}\ s^{-1}$).[10,14] However, although efforts have been made on the transverse thermoelectric properties of topological semimetal materials, a simple and effective way to manipulate the performance of transverse thermoelectric materials still remains elusive.

In recent years, $Mg_{3+\delta}Bi_2$ has drawn intense attention as a promising thermoelectric material, exhibiting excellent performance in traditional thermoelectricity.[15] It has relatively low transverse thermoelectric performance, however, due to its low carrier mobility (~ 450 $cm^2\ V^{-1}\ s^{-1}$),[16,17] which has been attributed to the formation of Mg vacancy defects during the synthesis process.[18] Previously, we demonstrated that the defect engineering method (*i.e.* Fermi energy tuning) was effective in suppressing Mg vacancies and optimizing carrier mobility.[19] The electron mobility increased by an order of magnitude, boosting magnetoresistance (MR) by 940% and vastly improving both the transverse thermopower (127 $\mu V\ K^{-1}$) and transverse power factor (2182 $\mu W\ m^{-1}\ K^{-2}$) at 13.5 K and 6 Tesla, rendering the $Mg_{3+\delta}Bi_2$ a promising transverse thermoelectric material. However, two open questions remain. Is it possible to further boost the transverse thermoelectric effect by regulating the topological electronic structure in topological materials? If so, is there a simple way to search for new promising candidates?

Owing to the linear-dispersed bands of Dirac semimetals, their massless low-energy excitations can dramatically enhance the carrier mobility. Thus, a topological transition of $Mg_{3+\delta}Bi_2$ from a Z_2 topological insulator to a Dirac semimetal phase would be desirable. In this work, we report that the as-fabricated $Mg_{3+\delta}Bi_2$:Mn_x has a large transverse thermopower (617 $\mu V\ K^{-1}$ at 14 K and 14 Tesla) and power factor (20 393 $\mu W\ m^{-1}\ K^{-2}$ at 14 K and 14 Tesla), the highest value among the reported polycrystalline transverse thermoelectric materials. The vastly improved electronic mobility (35 280 $cm^2\ V^{-1}\ s^{-1}$ at 2 K) and MR (16 600% at 2 K and 14 Tesla) outperformed the defect-engineering-optimized $Mg_{3+\delta}Bi_2$ by 7 and 17 times, respectively. Through first-principles calculations of pristine and doped $Mg_{3+\delta}Bi_2$, we verified the topological phase transition from a Z_2 topological insulator to a Dirac semimetal *via* Mn doping as a result of the combined effects of the negative chemical pressure and disorder effect (Fig. 1(A)). As anticipated, our MR measurements and transport calculations also showed a clear positive relation between transverse thermopower and MR. Our work provides a technical route for exponentially boosting transverse thermoelectricity through the direct engineering of topological electronic structures and identifies high non-saturated MR as a critical feature of promising candidates for future high-performance transverse thermoelectric materials.

2. Results and discussion

2.1. Giant transverse thermoelectric effect

The as-fabricated polycrystalline Mn-doped material is denoted as $Mg_{3+\delta}Bi_2$:Mn_x (x = 0, 0.025, 0.075, 0.1, 0.125, 0.15; δ indicates Mg-rich condition), which was synthesized by combined mechanical alloying and spark plasma sintering.[19] The nominal compositions of these samples are presented in Table S1 (ESI†). The Rietveld refinements of the as-fabricated $Mg_{3+\delta}Bi_2$:Mn_x samples with a space group of $P\bar{3}m1$ showed that both the a axis and c axis increased with the Mn content (Fig. 1(B)), and the corresponding cell volume V gradually increased from 137.8 $Å^3$ to 142.8 $Å^3$ as the Mn content increased from x = 0 to x = 0.15. The detailed Rietveld refinements are presented in the ESI† (Fig. S2 and Tables S2–S5). Based on the formation energy calculation (Fig. S3, ESI†), Mn prefers the Mg tetrahedron site (1/3, 2/3, 0.631). The ionic size of Mn (0.066 nm) at the tetrahedron site is larger than the Mg (0.057 nm), and hence the Mn dopant expanded the lattice, inducing negative chemical pressure in the $Mg_{3+\delta}Bi_2$ matrix. We believed that the negative chemical pressure could be similar to tensile strain, inducing a topological transition from a Z_2 topological insulator into a Dirac semimetal. The temperature-dependent transverse thermopower of the as-fabricated $Mg_{3+\delta}Bi_2$:Mn_x (x = 0.1) polycrystalline bulk under different magnetic fields (H) exhibits a peak near 14 K (Fig. 1(C)). The peak value increases up to 617 $\mu V\ K^{-1}$ at 14 Tesla, which is 5 times higher than that reported for polycrystalline $Mg_{3+\delta}Bi_2$[19] and also much higher than the peak values reported for other polycrystalline transverse thermoelectric materials (Fig. 1(D)).[8,11,20–24]

Fig. 1(E) further compares the transverse power factor (maximum output power density in practical applications[25]) of the as-fabricated $Mg_{3+\delta}Bi_2$:Mn_x (x = 0.1) polycrystalline bulk with reported transverse thermoelectric materials. For transverse thermoelectric materials, the transverse power factor was defined as $PF_T = S_T{}^2\sigma$, where S_T is the transverse thermopower perpendicular to the temperature gradient and σ is the regular electrical conductivity. Since S_T and σ usually have an opposite correction to the magnetic field strength, the PF_T showed a magnetic-field-dependent peak (Fig. S4, ESI†). In our investigated range (0–14 Tesla), the as-fabricated $Mg_{3+\delta}Bi_2$:$Mn_{0.1}$ showed a maximum value of 20 393 $\mu W\ m^{-1}\ K^{-2}$ under a 6 Tesla magnetic field, which was almost an order of magnitude higher than the 2182 $\mu W\ m^{-1}\ K^{-2}$ value reported for the $Mg_{3+\delta}Bi_2$ sample.[19] This value was also much higher than that of all polycrystalline materials and most single-crystal materials reported to date, including the Dirac semimetals $ZrTe_5$, $PtSn_4$,[11] $Pb_{0.77}Sb_{0.23}Se$,[20] Cd_3As_2,[8] and NbP;[10,13,14,26] the semimetals Mg_2Pb[21] and $Bi_{77}Sb_{23}$;[22] and the narrow-band semiconductors $Ag_{2(1+x)}Se$[23] and Re_4Si_7.[24] We also note that this value is still lower than that for the single-crystal Weyl semimetal WTe_2.[27,28] The polycrystalline $Mg_{3+\delta}Bi_2$:$Mn_{0.1}$, however, had obvious advantages in the preparation of large-size bulk and easy

 This journal is © The Royal Society of Chemistry 2023

Published on 10 February 2023. Downloaded by SUSTech on 3/1/2023 1:30:54 AM.

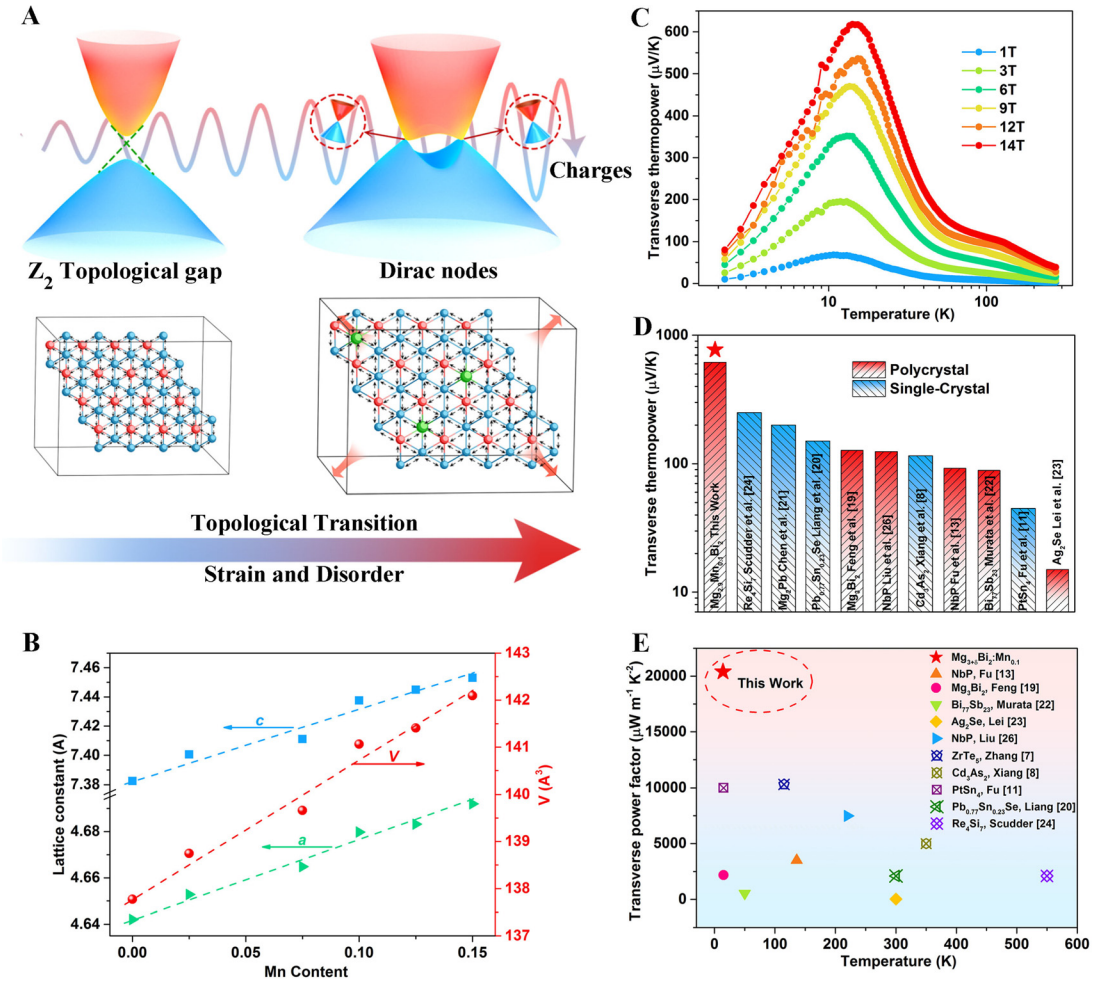

Fig. 1 Transverse thermoelectric performance of polycrystalline $Mg_{3+\delta}Bi_2$:Mn_x (x = 0.1). (A) A schematic of the topological phase transition of $Mg_{3+\delta}Bi_2$:Mn_x from a Z_2 topological insulator to a Dirac semimetal, resulting from the combined effects of negative chemical pressure and disorder. (B) The a axis, c axis and cell volume of the obtained Mn-doped samples according to the Rietveld refinements with a space group of $P\bar{3}m1$. (C) Transverse thermopower under different magnetic fields in a temperature range of 2–275 K. (D) A transverse thermopower comparison diagram of promising polycrystalline (red) and partial single-crystal (blue) materials. (E) A transverse power factor comparison diagram among promising transverse thermoelectric materials, where the filled and unfilled symbols represent polycrystalline and single-crystal materials, respectively.

regulation of the Fermi level, thus showing a promising realistic application.

2.2. An inverse relationship between S_T and σ under a magnetic field

Classic thermoelectric materials are characterized by a carrier concentration-dependent inversion between S and σ,[29] and transverse thermoelectric materials are similarly characterized by the magnetic field strength, which also connects the S_T and σ. As the charge carriers diffuse along the temperature gradient, the Lorentz force bends the trace of the charge flux due to the magnetic field—that is, the stronger the magnetic field, the larger the transverse charge flux, resulting in a higher transverse thermopower. For the σ, a stronger magnetic field leads to less charge carrier transport along the longitudinal direction, corresponding to decreased J_L (Fig. 2(A)). To verify the inverse relationship between S_T and σ, we measured the MR of the as-fabricated $Mg_{3+\delta}Bi_2$:Mn_x under different magnetic fields. Fig. 2(B) shows a magnetic-field-dependent MR of the $Mg_{3+\delta}Bi_2$:$Mn_{0.1}$ sample at different temperatures (2–300 K). Unsurprisingly, the MR at each temperature follows a nearly linear unsaturated trend in the high magnetic field range (B > 5 Tesla), which was consistent with the previously reported $Mg_{3+\delta}Bi_2$ sample[19] and the Dirac semimetals $Pb_{1-x}Sn_xSe$ and Cd_3As_2.[8,22] The corresponding MR of other as-fabricated $Mg_{3+\delta}Bi_2$:Mn_x are shown in Fig. S5 (ESI†). Fig. 2(C) plots the MR of $Mg_{3+\delta}Bi_2$:Mn_x at 2 K and 14 Tesla as a function of the Mn content, showing a dramatic increase in MR from 940% (x = 0) to a peak at 16 600% (x = 0.1), followed by a slight decrease to 10 300% (x = 0.15). These significant changes suggest that the chemical pressure caused by the Mn dopant alters the topology of the electronic structure.

Fig. 2(D)–(F) show the magnetic-field-dependent transverse thermoelectric properties of the as-fabricated $Mg_{3+\delta}Bi_2$:Mn_x (x = 0.025, 0.1, 0.15), which demonstrated similar magnetic-field-dependent behavior. As the magnetic-field increased from 0 to

Published on 10 February 2023. Downloaded by SUSTech on 3/1/2023 1:30:54 AM.

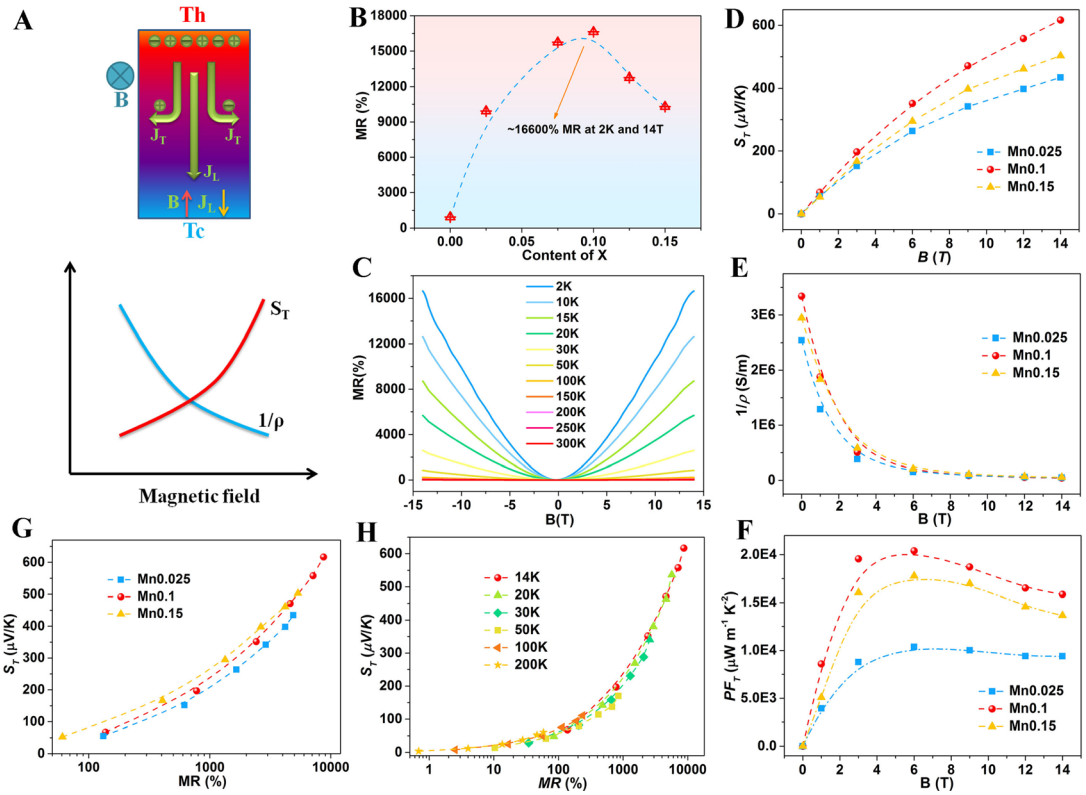

Fig. 2 Inverse relationship between S_T and σ. (A) A diagram of transverse thermoelectricity and the inverted relationship between S_T and $1/\rho$. (B) The MR of $Mg_{3+\delta}Bi_2$:$Mn_{0.1}$ at different temperatures in a magnetic field between −14 and 14 Tesla. (C) The Mn content-dependent MR of the as-fabricated polycrystalline $Mg_{3+\delta}Bi_2$:Mn_x ($0 \leq x \leq 0.15$) at 2 K and 14 Tesla. The magnetic field-dependent (D) S_T, (E) $1/\rho$, and (F) PF_T for $Mg_{3+\delta}Bi_2$:Mn_x (x = 0.025, 0.1, 0.15). The relationship between S_T and MR for (G) $Mg_{3+\delta}Bi_2$:Mn_x (x = 0.025, 0.1, 0.15) samples at 14 K and for (H) $Mg_{3+\delta}Bi_2$:$Mn_{0.1}$ under different temperatures.

14 Tesla, the S_T increased from 0 μV K^{-1} for all $Mg_{3+\delta}Bi_2$:Mn_x to 435 μV K^{-1} ($Mg_{3+\delta}Bi_2$:$Mn_{0.025}$), 617 μV K^{-1} ($Mg_{3+\delta}Bi_2$:$Mn_{0.1}$), and 503 μV K^{-1} ($Mg_{3+\delta}Bi_2$:$Mn_{0.15}$), respectively. The $Mg_{3+\delta}Bi_2$:$Mn_{0.1}$ sample exhibited the highest transverse thermopower in the whole magnetic field range. Unlike the S_T, the $1/\rho$ gradually decreased with the magnetic field for $Mg_{3+\delta}Bi_2$:Mn_x (x = 0.025, 0.1, 0.15) samples (Fig. 2(E)), which we attribute to the deflection of carriers by Lorentz force. Using the results of the magnetic-field-dependent S_T and $1/\rho$, we calculated the PF_T. Fig. 2(F) plots the magnetic-field-dependent PF_T for all three samples, which initially increased and then decreased, reaching the highest PF_T values at 6 Tesla: 10 370 μW m^{-1} K^{-2} ($Mg_{3+\delta}Bi_2$:$Mn_{0.025}$), 20 393 μW m^{-1} K^{-2} ($Mg_{3+\delta}Bi_2$:$Mn_{0.1}$), and 17 776 μW m^{-1} K^{-2} for $Mg_{3+\delta}Bi_2$:$Mn_{0.15}$.

Fig. 2(G) shows a clear positive correlation between S_T and MR for $Mg_{3+\delta}Bi_2$:Mn_x samples with different Mn content at 14 K. For $Mg_{3+\delta}Bi_2$:$Mn_{0.025}$, the S_T increased from 55 μV K^{-1} (132% MR) to 435 μV K^{-1} (4900% MR); for $Mg_{3+\delta}Bi_2$:$Mn_{0.1}$, the S_T increased from 68 μV K^{-1} (138% MR) to 617 μV K^{-1} (8710% MR); and for $Mg_{3+\delta}Bi_2$:$Mn_{0.15}$, the S_T increased from 52 μV K^{-1} (60% MR) to 503 μV K^{-1} (5350% MR). The MR-dependent S_T under different temperatures for the $Mg_{3+\delta}Bi_2$:$Mn_{0.1}$ sample (Fig. 2(H)) shows a similar correlation, which further solidifies the inverse relationship present between S_T and $1/\rho$ under a magnetic field.

2.3. Topological phase transition induced by Mn doping

We next performed first-principles calculations[19,30–33] to illustrate that the significantly enhanced transverse thermoelectric performance originated from the negative chemical pressure and disorder effect upon Mn doping. Fig. 3(A) and (B) show the topological phase transition of pristine Mg_3Bi_2 under 1% tensile strain. Without spin–orbit coupling (SOC), Mg_3Bi_2 is a type-II nodal-line semimetal with a nodal ring in the k_x–k_y plane, whereas SOC opens a small gap (*i.e.*, about 30 meV) around the nodal line (see Fig. 3(A)).[19,34–36] The band component projections of the Mg-s orbitals (red dots) and the Bi-p orbitals (blue dots) characterized a clear band inversion between the Γ_8^+ bands and the Γ_9^- bands at the Γ point,[37,38] where "+" and "−" indicate the parities of the Bloch wavefunctions. Based on the calculation of the evolution of the Wannier charge center for the six time-reversal invariant $\vec{k}$ planes (see Fig. S9, ESI†),[39] the bulk Z_2 topological number was characterized as [1,000]. Thus, a strong topological insulator phase of Mg_3Bi_2 was demonstrated.

According to the X-ray diffraction measurements, the lattice constants enlarged with the Mn doping (Fig. 1(B)), which is consistent with the fact that the ionic radius of Mn^{2+} is larger than that of Mg^{2+}. We then investigated the electronic structure of pure Mg_3Bi_2 under homogeneous tensile strains (Fig. 3(A)–(D), (G))

 This journal is © The Royal Society of Chemistry 2023

Published on 10 February 2023. Downloaded by SUSTech on 3/1/2023 1:30:54 AM.

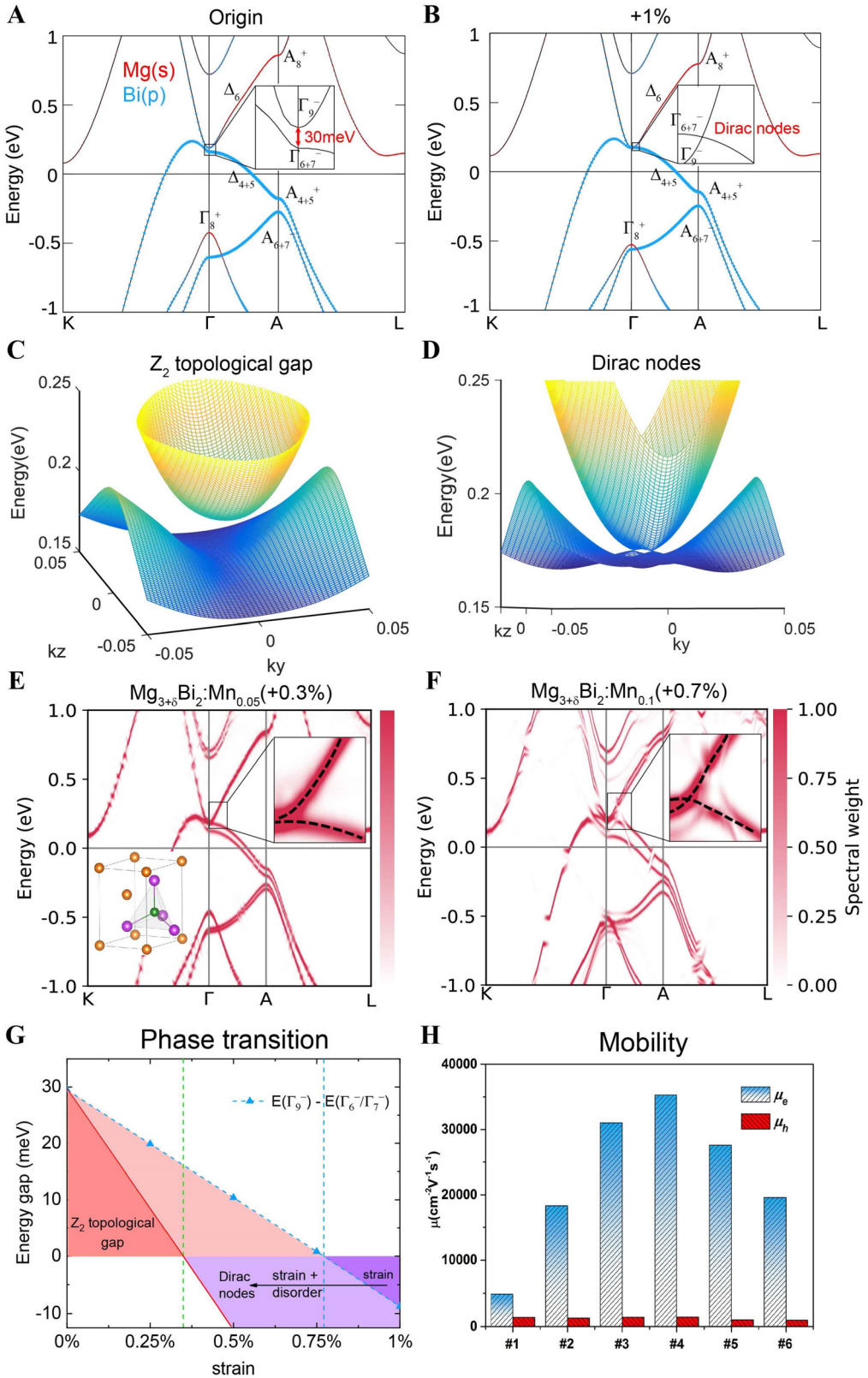

Fig. 3 Topological phase transition of $Mg_{3+\delta}Bi_2$:Mn_x. Band structures of pristine Mg_3Bi_2 with SOC for (A) original and (B) 1% tensile strain structures, with Mg-s components (red dots), Bi-p components (blue dots), and irreducible representations and parities also shown. Band evolution of the k_x = 0 plane from (C) original to (D) 1% tensile strain. Effective band structures of (E) $Mg_{3+\delta}Bi_2$:$Mn_{0.05}$ and (F) $Mg_{3+\delta}Bi_2$:$Mn_{0.1}$ with a tensile strain of 0.3% and 0.7%, respectively. (G) The energy differences between the Γ_9^- and Γ_{6+7}^- bands of Mg_3Bi_2, showing an increase in the tensile strain (blue dashed line), and the combined effects of the negative chemical pressure and disorder effect in $Mg_{3+\delta}Bi_2$:Mn_x (red line), which accelerates the topological phase transition. (H) Electron and hole mobilities for $Mg_{3+\delta}Bi_2$:Mn_x with various Mn contents.

Published on 10 February 2023. Downloaded by SUSTech on 3/1/2023 1:30:54 AM.

to simulate the negative chemical pressure. With an increase in the tensile strain from 0% to 0.25%, 0.50%, and 0.75%, the Γ_9^- bands at the Γ point continuously shifted down and the band gaps between the Γ_9^- and Γ_{6+7}^- bands decreased from ~30 to 20, 10 and 0.8 meV, respectively (the sloping blue dashed line in Fig. 3(G)). Under 1% tensile strain, the Γ_9^- bands finally crossed the Γ_{6+7}^- bands, forming a type-I Dirac point along the Γ–A line (Fig. 3(B) and (D), and Fig. S10, ESI†). The critical tensile strain of the topological phase transition was slightly larger than 0.75% (the vertical blue dashed line in Fig. 3(G)). The band evolution of the $k_x = 0$ plane from the undoped system (Fig. 3(C)) to the 1% tensile strain (Fig. 3(D)) clearly exhibited the emergence of Dirac points along the k_z direction, which was an accidental degeneracy protected by the C_3 rotational symmetry (Fig. S10, ESI†).

In addition to lattice expansion, the external chemical doping also introduced a disorder effect, *e.g.*, changing the electronic structure and Berry curvature by broadening the bands in topological semimetals.[40] The Mn dopants bring disorder effects, such as translational symmetry breaking and local lattice distortions. Leveraging the experimental lattice constants and the corresponding Mn contents, we investigated the disorder effect of Mn dopant by adopting supercell density functional theory (DFT) calculations with all atoms fully relaxed for $Mg_{3+\delta}Bi_2$:Mn_x (Fig. 3(E) and (F)). As shown in the inset of Fig. 3(E), the band crossing occurred in $Mg_{3+\delta}Bi_2$:$Mn_{0.05}$ at 0.3% lattice expansion. At a higher doping concentration, *i.e.*, $Mg_{3+\delta}Bi_2$:$Mn_{0.1}$ with a 0.7% lattice expansion (Fig. 3(F)), a clear band crossing occurred along the Γ–A line (black dashed line in the inset of Fig. 3(F)). This result suggests that the disorder effect (*i.e.*, band broadening) further accelerated the topological phase transition from a Z_2 topological insulator to a Dirac semimetal by decreasing the critical lattice constant. We also note that the introduction of a local magnetic moment of Mn breaks the time-reversal symmetry, splitting the energy bands. At a low doping level, this splitting is small and the competing disorder effect that broadening the energy bands can maintain the Dirac band feature. The enlarged purple area of the Dirac semimetal in the phase diagram (Fig. 3(G)) describes the combined effect of negative chemical pressure and disorder of the Mn dopant, giving rise to low-energy massless excitations around Dirac points with an ultrahigh Fermi velocity and thus a high electron mobility. In contrast, the hole pocket remains almost unchanged during the topological phase transition (Fig. 3(E) and (F)).

According to the band structure of pristine Mg_3Bi_2 (Fig. 3(A)) and the effective band structure of $Mg_{3+\delta}Bi_2$:$Mn_{0.1}$ (Fig. 3(F)), the band features around K, A and L points change little, and the Fermi velocities should remain almost unchanged. The main change of electronic structure after Mn doping is the topological phase transition from the Z_2 topological gap to Dirac nodes around the Γ point, which dramatically changes the Fermi velocity of electrons. This fact also agrees with our experimental results that the mobility of electrons but not holes is enhanced during the Mn doping (Fig. 3(H)). We also measure the carrier concentrations of $Mg_{3+\delta}Bi_2$:Mn_x with different Mn contents (Fig. S11, ESI†), indicating an almost fixed Fermi level. This is due to the fact that the valence states of Mn and Mg at the tetrahedral site are both +2, and no extra electrons are introduced to change the Fermi level. Overall, we attribute both the giant electron mobility and the enhanced thermoelectric performance in Mn-doped $Mg_{3+\delta}Bi_2$ to the topological phase transition from a Z_2 topological insulator to a Dirac semimetal. We calculated the transverse zT value for the obtained $Mg_{3+\delta}Bi_2$:$Mn_{0.1}$ sample at 6 Tesla and the best zT is 0.025 at 15 K, which is comparable with the state-of-the-art transverse thermoelectric materials, such as single-crystal $NbSb_2$ (zT = 0.1, at 25 K),[42] $PtSn_4$ (zT = 0.01, at 15 K),[11] Mg_2Pb (zT = 0.01, at 25 K),[21] $YbMnBi_2$ (zT = 0.002, at 175 K),[6] *etc.* (Fig. S12, ESI†).

2.4. Enhanced MR and transverse thermopower

Based on the Boltzmann transport method, we theoretically investigated the MR of Mn-doped $Mg_{3+\delta}Bi_2$ as a function of the external magnetic field: $\mathrm{MR} = \frac{\rho(\boldsymbol{B}) - \rho(0)}{\rho(0)} \times 100\%$, where $\rho(\boldsymbol{B})$ is the electrical resistivity (see Methods in the ESI†). The Fermi level is set at the Dirac points of the effective band structure, *i.e.*, $E_f \approx 0.25$ eV, where the carrier mobility is expected to be the highest (Fig. 3(F)). Fig. 4(A) and (B) show the MR behaviors of $Mg_{3+\delta}Bi_2$:$Mn_{0.1}$ with an external magnetic field along the x and z directions, obtained from a $3 \times 3 \times 1$ supercell. We found that the z-axis MR exhibited non-saturating behavior when the magnetic field was along the x-direction (*i.e.*, $B \| x$), reaching 25 000%; in contrast, the x-axis and y-axis MR were significantly smaller and rapidly saturated with $B \| x$ (Fig. 4(A)). When $B \| z$, the MR along the x and y directions degenerated, owing to the in-plane rotational symmetry. In contrast to those of pristine Mg_3Bi_2, the x-axis and y-axis MR of $Mg_{3+\delta}Bi_2$:$Mn_{0.1}$ exhibited non-saturating behavior that reached 3000% (Fig. 4(B)). Thus, we predicted that the MR of $Mg_{3+\delta}Bi_2$:$Mn_{0.1}$ was one order of magnitude higher than the MR of pristine Mg_3Bi_2, which was consistent with our experimental results from the polycrystalline samples (Fig. 2(C)). The MR is enhanced for two reasons: the increase of mobility (and, hence, longer relaxation time τ) due to the topological phase transition, and the band broadening caused by the disorder effect of the Mn doping.

The transverse thermopower is closely related to the MR, so, without a loss of generality, we considered a case where the temperature gradient was along the x direction (*i.e.*, $\nabla_x T \neq 0$, $\nabla_y T = \nabla_z T = 0$) and the magnetic field $\boldsymbol{B}$ was along the z direction. The transverse electrical conductivity σ_{xy} was generally several orders of magnitude smaller than the longitudinal terms σ_{xx} and σ_{yy}. Thus, the transverse thermopower S_T can be simplified as $S_T \approx \alpha_{yx}/\sigma_{yy} \approx \alpha_{yx}\rho_{yy}$, where α and ρ are the thermoelectrical conductivity and the electrical resistivity, respectively. Due to the positive relation between transverse thermopower S_T and MR, we naturally expected a huge thermopower enhancement of $Mg_{3+\delta}Bi_2$:$Mn_{0.1}$ since the one-order-of-magnitude enhancement of MR was verified. We also examined the general relationship between S_T and MR in other reported materials (Fig. 4(C)), which further supports our conclusion that a huge MR induces a giant transverse thermopower. Thus,

 This journal is © The Royal Society of Chemistry 2023

Published on 10 February 2023. Downloaded by SUSTech on 3/1/2023 1:30:54 AM.

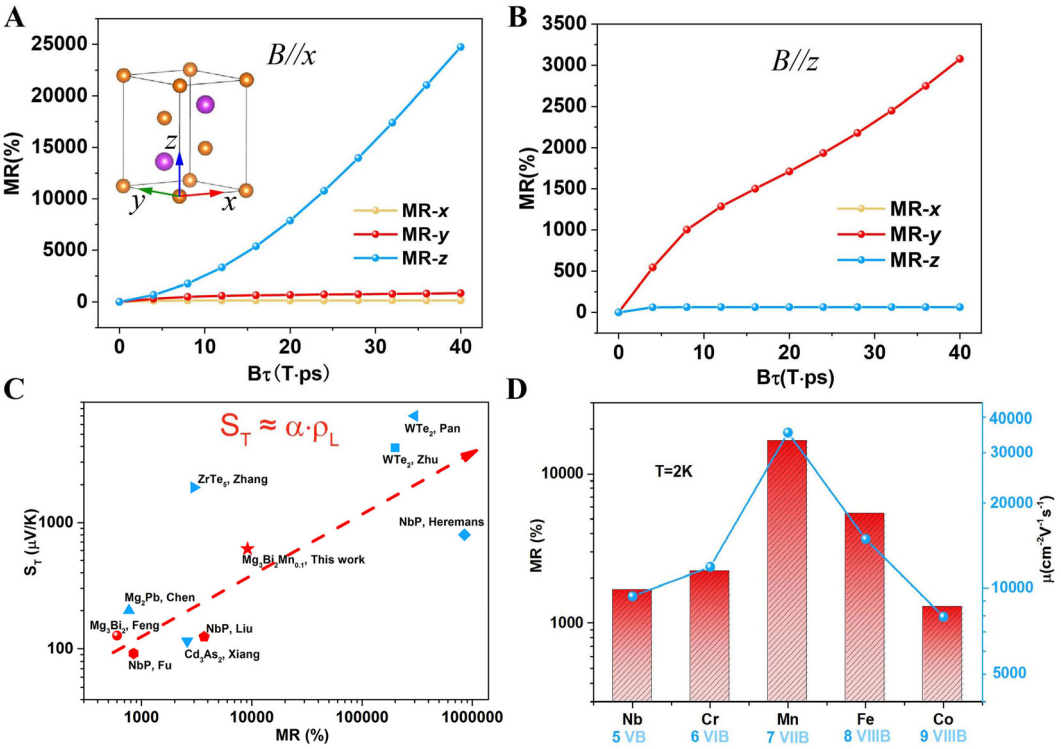

Fig. 4 Enhanced MR and positive relationship between MR and S_T. MR behaviors of $Mg_{3+\delta}Bi_2$:$Mn_{0.1}$ with the external magnetic field along the (A) *x* and (B) *z* directions. The maximum Bτ is set as 40 (T ps), due to a relaxation time larger than that of pristine Mg_3Bi_2. MR-*x* and MR-*y* are degenerate for B∥*z* owing to the in-plane rotational symmetry. (C) The generally positive relationship between transverse thermopower S_T and MR for various systems with polycrystalline (red) and single-crystal (blue) materials. (D) The MR (left) and carrier mobilities (right) of $Mg_{3+\delta}Bi_2$:$M_{0.1}$ doped with various transition elements (*i.e.*, M = Nb, Cr, Mn, Fe, Co).

the ongoing search for novel high-performance transverse thermoelectric materials could use the high MR as a quick screen indicator.

To further verify the relationship between the MR and the topological phase transition induced by ionic chemical pressure, we selected four extra transition elements (Nb, Cr, Fe, and Co) with different ionic radii for doping and compared these samples with the $Mg_{3+\delta}Bi_2$:$Mn_{0.1}$. As the doped element evolved from Nb in the 5th group to Co in the 9th group, the MR of $Mg_{3+\delta}Bi_2$:$M_{0.1}$ (M = Nb, Cr, Mn, Fe, Co) started at 1652% (M = Nb), peaked at 16 600% (M = Mn), and then decreased to 1274% (M = Co) (Fig. 4(D)). We measured and fit the Hall resistivity (Fig. S13, ESI†) to determine the electron mobility of these five transition-element-doped samples (Fig. 4(D)). As expected, the electron mobility and MR follow a similar trend, reaching a maximum value for M = Mn. This result is consistent with the situation discussed above in regard to the $Mg_{3+\delta}Bi_2$:Mn_x (x = 0–0.15) samples. Generally, a transition element is introduced in $Mg_{3+\delta}Bi_2$ in the following two cases: (1) to form a four-coordination style at the internal Mg2 position and (2) to form a six-coordination style at the vertex Mg1 and the interstitial positions. The ionic radius for both the four- and six-coordination states of these five different transition elements are shown in Fig. S14 (ESI†).[41] Notably, the Nb and Cr elements only existed in the form of six-coordination in the crystal. Our results indicate a strong correlation between changes in the ion radius and changes in both electron mobility and MR, regardless of whether the transition elements were distributed in the form of four- or six-coordination states in $Mg_{3+\delta}Bi_2$. These results further confirm the fact that the lattice expansion induces topological phase transition and improves both the electron mobility and MR in polycrystalline Mg_3Bi_2-based materials.

We also measured the *M*–*T* curves of $Mg_{3+\delta}Bi_2$, $Mg_{3+\delta}Bi_2$:$Zn_{0.1}$ and $Mg_{3+\delta}Bi_2$:$Mn_{0.1}$ (as shown in Fig. S15, ESI†). Obviously, these three samples show a similar magnetic behavior with ferromagnetic–paramagnetic transition temperature around 180 K. Combined with the *M*–*H* curve (Fig. S16, ESI†), the magnetism behaviors remain almost unchanged between these samples, indicating that introducing a small amount of Mn atom in $Mg_{3+\delta}Bi_2$ has little effect on magnetic order. In this work, the as-fabricated samples were synthesized through mechanical alloying and spark plasma sintering. The raw materials were first loaded into a stainless-steel ball milling jar with two stainless steel balls and ball milled for 8 hours. During this process, trace amounts of Fe might enter the samples, which may be responsible for the weak magnetic moment in $Mg_{3+\delta}Bi_2$, $Mg_{3+\delta}Bi_2$:$Zn_{0.1}$ and $Mg_{3+\delta}Bi_2$:$Mn_{0.1}$. Thus, the improved performance of Mn-doped samples in this work is mainly attributed to the high mobility caused by the topological electronic structure transition, rather than magnetic order.

Finally, transverse thermoelectric materials have great potential in thermoelectric energy conversion, especially in

Published on 10 February 2023. Downloaded by SUSTech on 3/1/2023 1:30:54 AM.

low-temperature refrigeration or thermal management. Recently, researchers suggested that the specific heat pumping powers of transverse thermoelectric materials are higher than those of liquid hydrogen and liquid nitrogen.[21,42] Additionally, compared with longitudinal thermoelectric devices, the transverse thermoelectric devices do not need both n and p types of thermoelectric materials for constructing one device, which significantly simplifies the thermoelectric module. The main problem in the future is that transverse thermoelectric materials still need a high magnetic field to achieve high performance. Therefore, realizing high transverse thermoelectric performance under low magnetic field or even zero magnetic field (anomalous Nernst effect) will be one of the research directions for broad applications.

3. Conclusion

In summary, we observed a remarkable transverse thermoelectric effect in a polycrystalline Dirac semimetal Mn-doped $Mg_{3+\delta}Bi_2$. The introduction of a Mn element induced lattice expansion and disorder effect and promoted a topological phase transition towards the Dirac semimetal, rendering the highest MR (16 600%) and electron mobility (35 280 $cm^2 V^{-1} s^{-1}$) in $Mg_{3+\delta}Bi_2$:$Mn_{0.1}$. Remarkably, the transverse thermopower reached 617 $\mu V K^{-1}$ at 14 K and 14 Tesla, the highest value currently recorded for a polycrystalline material, and the transverse power factor (20 393 $\mu W m^{-1} K^{-2}$) exceeds that of pristine $Mg_{3+\delta}Bi_2$ (2182 $\mu W m^{-1} K^{-2}$) by almost an order of magnitude. Our work offers a general experimental approach to engineering the transverse thermoelectric performance, using dopants to tune the chemical pressure and, in doing so, change the topological electronic structures near the Fermi surface. Our findings also highlight a generally positive relationship between transverse thermopower and MR, which will accelerate the rational design of novel transverse thermoelectric materials.

Author contributions

T. F. and W. L. designed this work. T. F. and Z. H. synthesized the samples. T. F. carried out the thermal transport property measurements and analyzed the results. T. F. and L. Z. carried out the electrical transport property measurements and analyzed the results. P. W. and Q. L. carried out the DFT calculations. W. Z. provided helpful discussion. T. F. and P. W. wrote the paper. All authors conceived the experiments, analyzed the results, and coedited the manuscript.

Conflicts of interest

The authors declare no conflicts of interest.

Acknowledgements

This work was supported by the National Key R&D Program of China (2019YFA0704900), National Natural Science Foundation of China (51872133), Shenzhen Key Program for Long-Term Academic Support Plan (20200925164021002), and Guangdong Innovative and Entrepreneurial Research Team Program (2017ZT07C062). The authors would like to thank the support of Core Research Facilities (SCRF) and Center for Computational Science and Engineering of Southern University of Science and Technology, and the support of Guangdong Provincial Key Laboratory Program (2021B1212040001 and 2019B030301001). W. S. L. acknowledges the support from the Tencent Foundation through the XPLORER PRIZE.

Notes and references

1 H. J. Goldsmid, *Introduction to Thermoelectricity*, Springer Press, Heidelberg, 2009.
2 A. Sakai, S. Minami, T. Koretsune, T. Chen, T. Higo, Y. Wang, T. Nomoto, M. Hirayama, S. Miwa, D. Nishio-Hamane, F. Ishii, R. Arita and S. Nakatsuji, *Nature*, 2020, **581**, 53–57.
3 C. M. Jaworski, R. C. Myers, E. Johnston-Halperin and J. P. Heremans, *Nature*, 2012, **487**, 210–213.
4 K. Behnia and H. Aubin, *Rep. Prog. Phys.*, 2016, **79**, 046502.
5 X. H. Chen, *Sci. China: Phys., Mech. Astron.*, 2020, **63**, 237031.
6 Y. Pan, C. Le, B. He, S. J. Watzman, M. Yao, J. Gooth, J. P. Heremans, Y. Sun and C. Felser, *Nat. Mater.*, 2022, **21**, 203–209.
7 W. Zhang, P. Wang, B. Skinner, R. Bi, V. Kozii, C. W. Cho, R. Zhong, J. Schneeloch, D. Yu, G. Gu, L. Fu, X. Wu and L. Zhang, *Nat. Commun.*, 2020, **11**, 1046.
8 J. S. Xiang, S. L. Hu, M. Lyu, W. Zhu, C. Ma, Z. Chen, F. Steglich, G. Chen and P. Sun, *Sci. China: Phys., Mech. Astron.*, 2020, **63**, 237011.
9 T. Liang, J. Lin, Q. Gibson, T. Gao, M. Hirschberger, M. Liu, R. J. Cava and N. P. Ong, *Phys. Rev. Lett.*, 2017, **118**, 136601.
10 S. J. Watzman, T. M. McCormick, C. Shekhar, S. C. Wu, Y. Sun, A. Prakash, C. Felser, N. Trivedi and J. P. Heremans, *Phys. Rev. B*, 2018, **97**, 161404.
11 C. G. Fu, S. N. Guin, T. Scaffidi, Y. Sun, R. Saha, S. J. Watzman, A. K. Srivastava, G. Li, W. Schnelle, S. S. P. Parkin, C. Felser and J. Gooth, *Research*, 2020, 4643507.
12 W. Y. Zhao, Z. Y. Liu, Z. G. Sun, Q. J. Zhang, P. Wei, X. Mu, H. Y. Zhou, C. C. Li, S. F. Ma, D. Q. He, P. X. Ji, W. T. Zhu, X. L. Nie, X. L. Su, X. F. Tang, B. G. Shen, X. L. Dong, J. H. Yang, Y. Liu and J. Shi, *Nature*, 2017, **549**, 247–251.
13 C. G. Fu, S. N. Guin, S. J. Watzman, G. Li, E. Liu, N. Kumar, V. Süβ, W. Schnelle, G. Auffermann, C. Shekhar, Y. Sun, J. Gooth and C. Felser, *Energy Environ. Sci.*, 2018, **11**, 2813–2820.
14 C. Shekhar, A. K. Nayak, Y. Sun, M. Schmidt, M. Nicklas, I. Leermakers, U. Zeitler, Y. Skourski, J. Wosnitza, Z. Liu, Y. Chen, W. Schnelle, H. Borrmann, Y. Grin, C. Felser and B. Yan, *Nat. Phys.*, 2015, **11**, 645–649.
15 J. Mao, H. Zhu, Z. Ding, Z. Liu, G. A. Gamage, G. Chen and Z. Ren, *Science*, 2019, **365**, 495–498.

 This journal is © The Royal Society of Chemistry 2023

Published on 10 February 2023. Downloaded by SUSTech on 3/1/2023 1:30:54 AM.

16 J. Xin, G. Li, G. Auffermann, H. Borrmann, W. Schnelle, J. Gooth, X. Zhao, T. Zhu, C. Felser and C. Fu, *Mater. Today Phys.*, 2018, **7**, 61–68.
17 T. Zhou, M. Tong, X. Xie, Y. Yu, X. Zhu, Z. Wang and T. Jiang, *J. Phys. Chem. Lett.*, 2020, **11**, 6475–6481.
18 S. Ohno, K. Imasato, S. Anand, H. Tamaki, S. D. Kang, P. Gorai, H. K. Sato, E. S. Toberer, T. Kanno and G. J. Snyder, *Joule*, 2018, **2**, 141–154.
19 T. Feng, P. S. Wang, Z. J. Han, L. Zhou, W. Q. Zhang, Q. H. Liu and W. S. Liu, *Adv. Mater.*, 2022, **34**, 2200931.
20 T. Liang, Q. Gibson, J. Xiong, M. Hirschberger, S. P. Koduvayur, R. J. Cava and N. P. Ong, *Nat. Commun.*, 2013, **4**, 2696.
21 Z. Chen, X. Zhang, J. Ren, Z. Zeng, Y. Chen, J. He, L. Chen and Y. Pei, *Nat. Commun.*, 2021, **12**, 3837.
22 M. Murata, K. Nagase, K. Aoyama and A. Yamamoto, *Appl. Phys. Lett.*, 2020, **117**, 103903.
23 Y. Z. Lei, W. Liu, X. Y. Zhou, J. F. Luo, C. Zhang, X. L. Su, G. J. Tan, Y. G. Yan and X. F. Tang, *J. Solid State Chem.*, 2020, **288**, 121453.
24 M. R. Scudder, B. He, Y. X. Wang, A. Rai, D. G. Cahill, W. Windl, J. P. Heremans and J. E. Goldberger, *Energy Environ. Sci.*, 2021, **14**, 4009.
25 W. S. Liu, H. S. Kim, S. Chen, Q. Jie, B. Lv, M. L. Yao, Z. S. Ren, C. P. Opeil, S. Wilson, C. W. Chu and Z. F. Ren, *Proc. Natl. Acad. Sci. U. S. A.*, 2015, **112**, 3269–3274.
26 W. Liu, Z. Wang, J. Wang, H. Bai, Z. Li, J. Sun, X. Zhou, J. Luo, W. Wang, C. Zhang, J. Wu, Y. Sun, Z. Zhu, Q. Zhang and X. Tang, *Adv. Funct. Mater.*, 2022, 2202143.
27 Z. Zhu, X. Lin, J. Liu, B. Fauqué, Q. Tao, C. Yang, Y. Shi and K. Behnia, *Phys. Rev. Lett.*, 2015, **114**, 176601.
28 Y. Pan, B. He, T. Helm, D. Chen, W. Schnelle and C. Felser, *Nat. Commun.*, 2022, **13**, 3909.
29 G. J. Snyder and E. S. Toberer, *Nat. Mater.*, 2008, **7**, 105–114.
30 N. W. Ashcroft and N. D. Mermin, *Solid State Physics*, Harcourt College Press, *FortWorth*, 1976.
31 J. M. Ziman, *Electrons and Phonons: The Theory of Transport Phenomena in Solids*, University Press, Oxford, UK, 2001.
32 S. N. Zhang, Q. S. Wu, Y. Liu and O. V. Yazyev, *Phys. Rev. B*, 2019, **99**, 035142.
33 Y. Liu, H. J. Zhang and Y. G. Yao, *Phys. Rev. B: Condens. Matter Mater. Phys.*, 2009, **79**, 245123.
34 T. R. Chang, I. Pletikosic, T. Kong, G. Bian, A. Huang, J. Denlinger, S. K. Kushwaha, B. Sinkovic, H. T. Jeng, T. Valla, W. Xie and R. J. Cava, *Adv. Sci.*, 2019, **6**, 1800897.
35 X. Zhang, L. Jin, X. Dai and G. Liu, *J. Phys. Chem. Lett.*, 2017, **8**, 4814–4819.
36 T. Zhou, X. Zhu, M. Tong, Y. Zhang, X. Luo, X. Xie, W. Feng, Q. Chen, S. Tan, Z. Wang, T. Jiang, Y. Tang, X. Lai and X. Yang, *Chin. Phys. Lett.*, 2019, **36**, 117303.
37 H. M. Weng, X. Dai and Z. Fang, *J. Phys.: Condens. Matter*, 2016, **28**, 303001.
38 J. C. Gao, Q. Wu, C. Persson and Z. J. Wang, *Comput. Phys. Commun.*, 2021, **261**, 107760.
39 Q. S. Wu, S. N. Zhang, H. F. Song, M. Troyer and A. A. Soluyanov, *Comput. Phys. Commun.*, 2018, **224**, 405–416.
40 J. Shen, Q. Yao, Q. Zeng, H. Sun, X. Xi, G. Wu, W. Wang, B. Shen, Q. Liu and E. Liu, *et al.*, *Phys. Rev. Lett.*, 2020, **125**, 086602.
41 R. D. Shannon, *Acta Crystallogr.*, 1976, **A32**, 751.
42 P. Li, P. Qiu, Q. Xu, J. Luo, Y. Xiong, J. Xiao, N. Aryal, Q. Li, L. Chen and X. Shi, *Nat. Commun.*, 2022, **13**, 7612.